nature nanotechnology

Supplementary information

https://doi.org/10.1038/s41565-026-02225-x

Computationally guided design of bioactive nanostructures for targeted clearance of amyloid-β aggregates in Alzheimer's disease

In the format provided by the authors and unedited

Table of contents

Supplementary Methods 2

In vivo biodistribution 2

In vivo therapeutic studies 2

Histological assessment 4

Single-cell RNA sequencing 6

Supplementary Figures 8

Supplementary Tables 27

Uncropped blots 30

References 31

Supplementary Methods

***In vivo* biodistribution**

200 μL of Cy5-labeled $_{A\beta3}FTn^{Au}$ (10 μM) was intravenously administered to 6-month-old WT and 5×FAD mice. At 1, 2, and 6 hours post-injection, the animals were sacrificed, and major organs including the brain were harvested for analysis. *Ex vivo* imaging was conducted at 6 hours post-injection using the IVIS Spectrum Imaging System (IVIS Lumina II Xenogen, Caliper Life Sciences). Nanoparticle accumulation in each organ was quantified by measuring the average fluorescence intensity within the region of interest (ROI). Brain tissues collected at 1, 2, and 6 hours post-injection were frozen, sectioned into 15 μm slices, and immunostained with a phycoerythrin (PE)-conjugated anti-mouse CD31 antibody (102508, BioLegend; 1:500) to visualize cerebral vasculature. Fluorescence imaging was performed using a LSM, with excitation/emission wavelengths set for nuclei (405/461 nm), blood vessels (565/578 nm), and $_{A\beta3}FTn^{Au}$ (633/670 nm). The depth of nanoparticle penetration into the HIP and PFC was assessed by the area ratio covered by NPs. Additionally, brain cryosections collected at 6 hours were co-stained with an anti-β-amyloid antibody (6E10, 803015; BioLegend; 1:1000) and Alexa Fluor 488-conjugated goat anti-mouse IgG (Ex/Em = 488/520 nm). The co-localization of NPs and Aβ plaques in the HIP and PFC regions was visualized using LSM.

To enable three-dimensional (3D) imaging analysis of the brain, 200 μL of Cy5-labeled $_{A\beta3}FTn^{Au}$ (10 μM) was intravenously injected into 6-month-old 5×FAD mice. The mice were sacrificed at 2 and 6 hours post-injection, and brain tissues were collected. Five minutes prior to tissues harvesting, blood vessels were labeled via intravenous injection of Lycopersicon esculentum (Tomato) lectin-Dylight 488. The brain samples were fixed in 4% paraformaldehyde at 4°C for 24 hours, followed by dehydration through a graded methanol series (20%-90% in PBS, 5 hours at room temperature). Tissues were then optically cleared in a benzyl alcohol/benzyl benzoate mixture (1:2, v/v) for 3-7 days in the dark, and subsequently washed at least three times with PBS. Light-sheet fluorescence microscopy (LaVision, BioTec) was used to image the cleared brain tissues, with excitation/emission wavelengths set at 488/525 nm for blood vessels and 633/670 nm for $_{A\beta3}FTn^{Au}$. Raw images were processed using the FIJI package in ImageJ 1.53t, and 3D reconstruction and quantitative analysis were performed using Imaris software 9.0.1.

***In vivo* therapeutic studies**

All animal experiments were conducted in accordance with the ethical guidelines and regulations approved by the Animal Ethics Committee of Hebei University of Technology

(HEBUTacuc2023010) and Nankai University (2024-SYDWLL-000198). The 5×FAD transgenic mice were obtained from The Jackson Laboratory. Age-matched wild-type littermates were used as controls where applicable. Mice were provided ad libitum access to food and water and housed in a specific pathogen-free environment with a 14 h light/10 h dark cycle, temperature of approximately 18-25°C and 40-60% humidity. Both male and female mice were used in behavioural and efficacy experiments, with sex balanced between groups or kept consistent within individual experiments. Six-month-old 5×FAD mice were randomly divided into four groups (n = 8 mice/group) and treated via intravenous injections with PBS, $_{A\beta3}$FTn, FTn^{Au}, or $_{A\beta3}$FTn^{Au} (5 mg/kg) every 4 days, for a total of 10 administrations. Age-matched wild-type littermates received PBS injections following the same schedule (n = 8 mice).

To evaluate cognitive function, behavioral tests including the Y-maze test, NOR test, and MWM were conducted. The Y-maze test was used to assess short-term working memory. Each mouse was placed individually into the maze and allowed to explore freely for 10 minutes. An automated tracking system recorded the sequence and total number of arm entries. Spontaneous alternation behavior, reflecting working memory, was calculated using the formula: Spontaneous Alternation (%) = (number of triads including entries into all three arms consecutively) / (total arm entries - 2) × 100. The NOR test assessed recognition memory. Mice were habituated to the testing arena the day before training and testing. Training phase: Mice were allowed to explore two identical objects for 10 minutes. Short-term memory test: Two hours later, one object was replaced with a novel one, and mice were allowed to explore for 5 minutes. Long-term memory test: After 24 hours, a new novel object and a familiar object were presented for 5 minutes. Exploration was defined as sniffing or direct contact with the objects. The RI was calculated using the formula: RI (%) = time spent exploring the novel object / (time spent on novel + familiar objects) × 100. To assess spatial learning and memory, the MWM test was performed using ANY-maze software (v7.16, Stoelting). The test consisted of two phases. Initial training (IT, Days 1-5): Mice were trained to find a hidden platform submerged 1.5 cm below the water surface in Quadrant I of a circular stainless-steel pool (120 cm diameter, 40 cm height, water depth 25 cm, maintained at 25 ± 1°C). The pool was divided into four quadrants (I-IV) aligned with cardinal directions (N, S, E, W). Each day, mice underwent 4 trials, with the drop location randomized among S, E, NE, and SW. Mice were allowed 60 seconds to locate the platform. If successful, they remained on the platform for 3 seconds. If unsuccessful, they were guided to the platform and remained for at least 10 seconds. Spatial exploration test (SET, Day 6): Twenty-four hours after the final IT session, a probe trial was conducted with the platform removed. Mice

were placed in the pool and allowed to swim for 60 seconds to assess spatial memory based on time spent in the target quadrant and number of crossings over the former platform location.

To evaluate biosafety, a series of *in vivo* assessments were conducted, including blood circulation, Au clearance, and blood parameter analyses. Specifically, blood circulation behavior was examined in 8-week-old female Kunming mice (n = 3 mice per group) by intravenous administration of fluorescently labeled nanomaterials, followed by collection of blood samples at multiple time points and measurement of plasma fluorescence intensity. To assess the metabolic clearance of gold, 6-month-old 5×FAD mice (n = 3 mice per time point) were intravenously injected with $_{A\beta3}FTn^{Au}$ at a dose five times higher than the therapeutic concentration. Mice were sacrificed at designated time points (6 hours, 3 days, and 7 days post-injection), and samples of the brain, liver, kidney, and blood were collected. Following acid digestion, the Au content in each tissue was quantified using ICP-OES. Systemic biosafety was further evaluated in 8-week-old female wild-type C57BL/6J mice using a dosing regimen consistent with the therapeutic schedule but at a threefold higher dose, followed by analysis of hematological parameters and plasma biochemical markers related to liver and kidney function. During the therapeutic study, body weight was recorded every 4 days throughout the treatment period, and all animals were monitored for signs of toxicity. At the end of the treatment, mice were euthanized by cervical dislocation, and major organs including the heart, liver, spleen, lungs, and kidneys, were collected. These organs were fixed in 4% paraformaldehyde, embedded in paraffin, sectioned at a thickness of 5 μm, and stained with H&E using a modified H&E stain kit (G1121, Solarbio) for histopathological examination under a light microscope.

Histological assessment

To quantify soluble and insoluble human Aβ levels in brain tissue, ELISA was performed. HIP and PFC tissues from 6-month-old 5×FAD transgenic mice with or without treatment were subjected to sequential extraction. Soluble Aβ was isolated using radioimmunoprecipitation assay (RIPA) buffer, while the insoluble fraction was subsequently extracted through denaturation with concentrated formic acid[1]. Both soluble and insoluble Aβ isoforms were quantified using commercially available and validated Human Amyloid beta (aa1–42) Quantikine ELISA Kit (DAB142, R&D). All assays were performed in accordance with the manufacturers' instructions. In addition, brain tissue sections were stained with the anti-β-amyloid antibody (6E10; 1:1000) to detect total Aβ, and with the anti-amyloid fibrils (OC; 1:100) antibody and ThT (3 g/L in 50% ethanol) as fibril-selective

indicators. Briefly, fixed sections were blocked and incubated with the primary antibody (6E10 or OC) followed by fluorescent secondary antibody, washed, and mounted for imaging. For ThT staining, fixed sections were incubated with ThT solution, washed, and mounted. Quantitative image analysis was conducted using ImageJ software 1.53t.

Electrophysiological recordings between the PP and the DG were performed after completion of the MWM tests. Mice were anesthetized with 30% urethane (1.2 g/kg body weight; Sigma-Aldrich) and positioned in a stereotaxic apparatus (SN-3, Narishige) for surgery. A midline scalp incision (~2 cm) was made to expose the skull, and two small craniotomies were drilled on the left hemisphere for electrode placement. Based on the coordinates from the mouse brain atlas, a concentric bipolar stimulating electrode was implanted into the PP (3.8 mm posterior to bregma, 3.0 mm lateral to midline, 1.5 mm ventral from the dura), and a recording electrode was inserted into the DG (2.0 mm anterior to bregma, 1.4 mm lateral to midline, 1.5 mm ventral from the dura). To determine the optimal stimulus intensity, test pulses (0.2 ms duration, 0.1–0.9 mA) were delivered to the PP every 30 seconds at 0.03 Hz, adjusted to evoke 70% of the maximal fEPSP response. A stable baseline was recorded for 20 minutes. LTP was then induced using a TBS protocol consisting of 30 trains of 12 pulses at 200 Hz, delivered at 5 Hz. Post-TBS recordings were conducted every 60 seconds for 1 hour to monitor LTP induction and maintenance.

Golgi staining was performed to assess potential changes in dendritic spine density within the DG region of the HIP. Following rapid extraction, brain tissues were immersed in Golgi staining solution and incubated at room temperature in the dark for 14 days. The staining solution was refreshed every two days to ensure optimal impregnation. On day 15, brains were sectioned coronally into 150 μm-thick slices using a vibrating blade microtome (Leica VT1000 S). The sections were sequentially processed through the following steps: immersion in 5% Na_2CO_3 for 20 minutes, rinsing with distilled water for 1 second, dehydration in 70% ethanol (10 minutes), 90% ethanol (15 minutes), and 100% ethanol (20 minutes), followed by clearing in xylene for 20 minutes. Finally, sections were mounted with neutral balsam for imaging. Straight terminal dendritic branches with clearly visible spines and a minimum length of 10 μm were selected for analysis. For each group, thirty dendritic segments were imaged and quantified using ImageJ 1.53t to determine spine density in the hippocampal DG region.

The expression levels of synaptic-related proteins were analyzed using standard Western blot experiments. The primary antibodies used include: anti-NMDAR2A antibody (ab169873, Abcam; 1:1000), PSD95-specific antibody (81106-1-RR, Proteintech; 1:5000), anti-synaptophysin antibody (ab52636, Abcam; 1:1000), ApoE antibody (66830-1-Ig,

Proteintech; 1:3000), and Trem2 (E7P8J) monoclonal antibody (76765, Cell Signaling Technology; 1:1000). To analyze the expression and distribution of synaptic-related proteins, immunofluorescence staining was performed using the following primary antibodies: Aβ oligomer A11 polyclonal antibody (AHB0052, Invitrogen; 1:500), ApoE antibody (66830-1-Ig, Proteintech; 1:500), Trem2 antibody (DF12529, Affinity Biosciences; 1:500), and PSD95 monoclonal antibody (BF8419, Affinity Biosciences; 1:300).

Single-cell RNA sequencing

Following treatment, hippocampal tissues were isolated from 6-month-old male 5×FAD mice treated with either PBS or $_{A\beta3}FTn^{Au}$, along with age-matched male WT littermates treated with PBS (n = 2 mice per group). Dissections were performed on ice, with careful attention to maintaining cell viability during tissue dissociation. Single-cell suspensions were prepared and adjusted to a concentration of 700–1200 viable cells per μL, as determined by a CellDrop FL Cell Counter. Using the Chromium Single Cell 3' GEM, Library & Gel Bead Kit v3.1 (10x Genomics, PN-1000268), the suspensions were loaded onto a Chromium Single Cell G Chip (PN-1000120) following the manufacturer's protocol. This enabled droplet-based co-encapsulation of individual cells with barcoded gel beads. Within each droplet, cells were lysed, and released mRNA was captured and barcoded during reverse transcription inside Gel Beads-in-Emulsion (GEMs). The resulting cDNA was synthesized and amplified using a T100 PCR Thermal Cycler (Bio-Rad) under the following conditions: 53 °C for 45 minutes, 85 °C for 5 minutes, and held at 4 °C. Amplified cDNA was quantified with a Qubit Fluorometer (Thermo Scientific) and quality-checked using the Bioanalyzer 2100 system (Agilent). Single-cell RNA sequencing libraries were then constructed according to the manufacturer's instructions and sequenced on an Illumina platform at a depth of approximately 40,000 reads per cell by Annoroad Gene Technology Co., Ltd.

For data processing, raw sequencing data were processed using Cell Ranger v.6.1.2 to generate expression matrices. Subsequent analyses were performed with the Seurat R package (v4.3.0.1). Low-quality cells were excluded based on the following criteria: fewer than 200 detected genes, more than 10,000 genes, or mitochondrial gene content exceeding 20%. Standard preprocessing steps—including normalization, identification of variable features, and data scaling—were carried out using Seurat's built-in functions (NormalizeData, FindVariableFeatures, and ScaleData) with default parameters. To mitigate batch effects across samples, we applied the Harmony integration algorithm. Dimensionality reduction and clustering were performed using the uniform manifold approximation and projection (UMAP), FindNeighbors, and FindClusters functions, with the resolution parameter set to

0.6. Cell types were annotated based on cluster-specific marker genes. Cell-cell communication analysis was conducted using the CellChat R package (v1.6.1) with default parameters. Ligand–receptor interactions among cell populations were used to infer intercellular communication networks, visualize interaction patterns, and identify key signaling pathways. For pathway enrichment analysis, the clusterProfiler R package (v4.6.2) was used to perform GOBP analysis. In addition, GSVA was conducted using the GSVA R package (v1.46.0). GO-based gene sets were used to calculate pathway activity scores for each cell subtype, and differential pathway activity was assessed by comparing GSVA scores across experimental conditions or cell populations.

Supplementary Figures

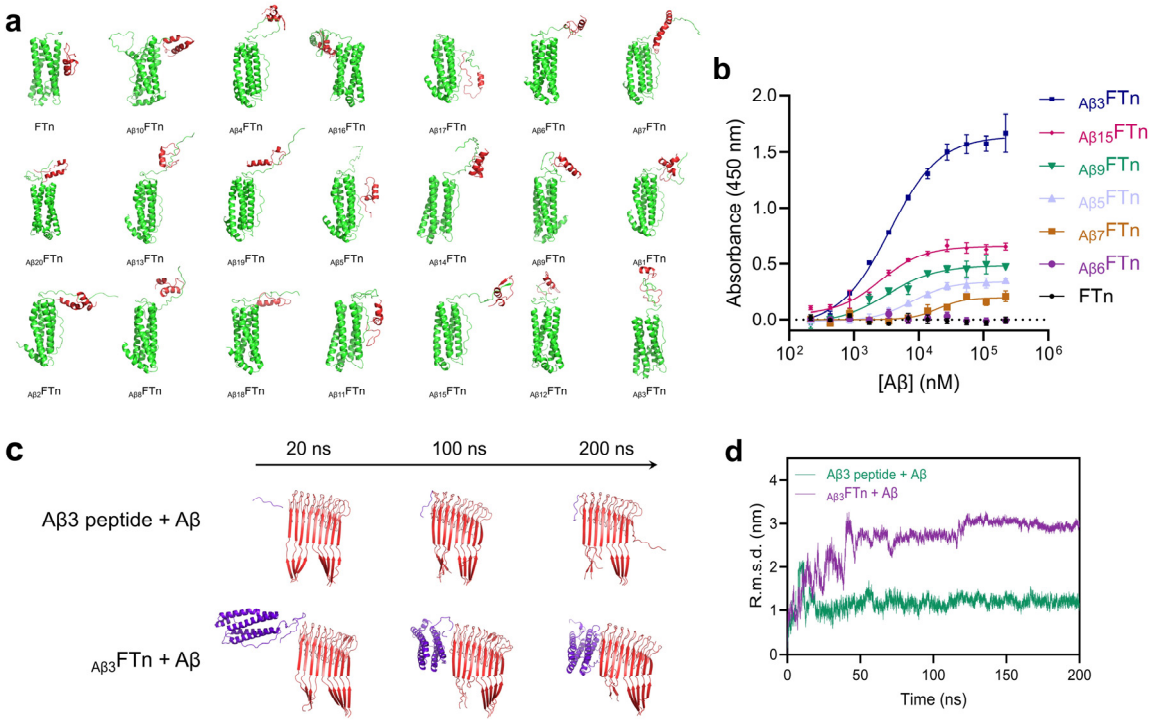

Supplementary Fig. 1. Computational analysis of $_{Aβ3}$FTn–Aβ interactions and binding dynamics. (**a**) Predicted molecular docking models showing Aβ (red) binding to wild-type FTn and its variants (green), with enhanced surface interactions observed in the modified constructs. (**b**) Sandwich ELISA quantification of binding affinities between $_{Aβ}$FTn and Aβ peptides. (**c**) Representative snapshots from time-resolved molecular dynamics simulations depicting interaction trajectories between Aβ and Aβ3 peptide (top) or the $_{Aβ3}$FTn subunit (bottom, purple). (**d**) RMSD profiles of the two systems over 200 ns of molecular dynamics simulations. Data in (**b**) are presented as mean ± SEM, based on three biologically independent experiments.

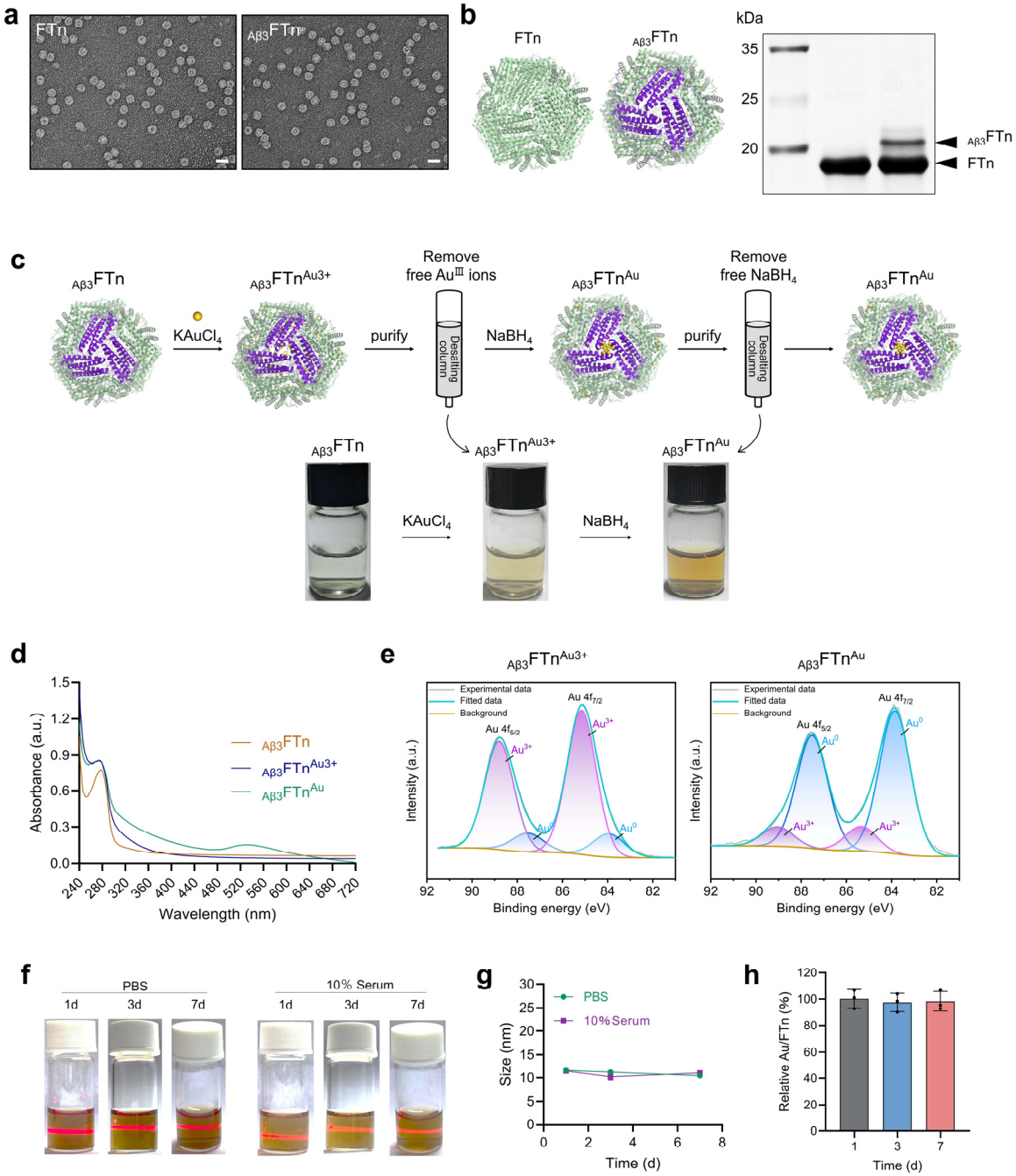

Supplementary Fig. 2. Characterization and physicochemical stability of Aβ3FTn constructs. (**a**) Representative TEM images of FTn and Aβ3FTn following negative staining with 1% uranyl acetate. Scale bar = 20 nm. (**b**) SDS–PAGE analysis showing protein band patterns of FTn and its engineered variants, indicating uniform subunit expression and successful modification. (**c**) Stepwise fabrication of Aβ3FTn^{Au}. Aβ3FTn was first incubated with $KAuCl_4$ to coordinate Au (III), followed by purification to remove unbound Au (III) ions. The coordinated Au (III) was then reduced by $NaBH_4$ and purified again to remove excess $NaBH_4$, yielding Aβ3FTn^{Au}. Photographs below the scheme show the progressive color change during coordination and reduction, supporting successful gold incorporation. (**d**) UV-vis absorption spectra of Aβ3FTn, Aβ3FTn^{Au3+}, and Aβ3FTn^{Au}. A distinct additional absorption feature appears in Aβ3FTn^{Au}, consistent with the formation of Au nanoclusters within the

ferritin nanocage. (**e**) XPS analysis of $_{A\beta3}FTn^{Au3+}$ and $_{A\beta3}FTn^{Au}$, showing a shift in Au signals consistent with the reduction of Au^{3+} to Au^{0} upon nanocluster formation. (**f**) Photographs of $_{A\beta3}FTn^{Au}$ dispersions in PBS and human serum-containing media after incubation for up to 7 days, showing a clear Tyndall effect without visible sedimentation or precipitation. (**g**) DLS measurements of $_{A\beta3}FTn^{Au}$ incubated in PBS and human serum-containing media over 7 days, showing no apparent change in hydrodynamic size distribution. (**h**) ICP-OES analysis of $_{A\beta3}FTn^{Au}$ after incubation in PBS for up to 7 days, indicating no detectable uncontrolled release of Au from the ferritin nanocage. Images in (**a**) are representative of three biologically independent experiments. Data in (**g**) and (**h**) are presented as mean ± SEM, based on three biologically independent experiments.

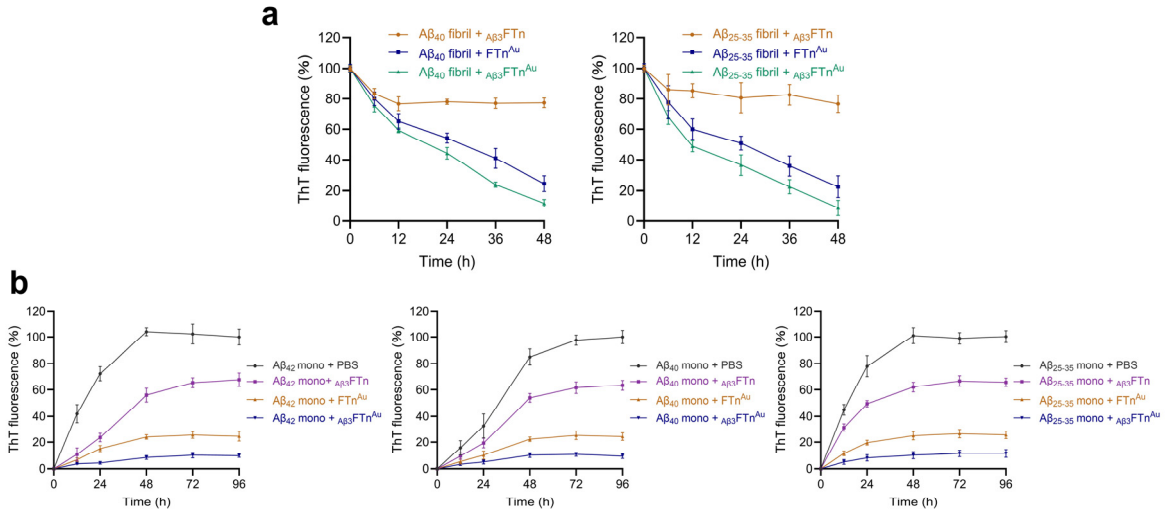

Supplementary Fig. 3. ThT fluorescence assays evaluating the effects of FTn-based NPs on the aggregation and disaggregation of different Aβ isoforms. (**a**) ThT fluorescence assay assessing the disaggregation of preformed $A\beta_{40}$ and $A\beta_{25\text{-}35}$ fibrils by different FTn-based NPs. (**b**) ThT fluorescence assay exploring the inhibition of spontaneous aggregation of $A\beta_{42}$, $A\beta_{40}$, and $A\beta_{25\text{-}35}$ in the presence of different FTn-based NPs. All values were presented as mean ± SEM, based on three biologically independent experiments.

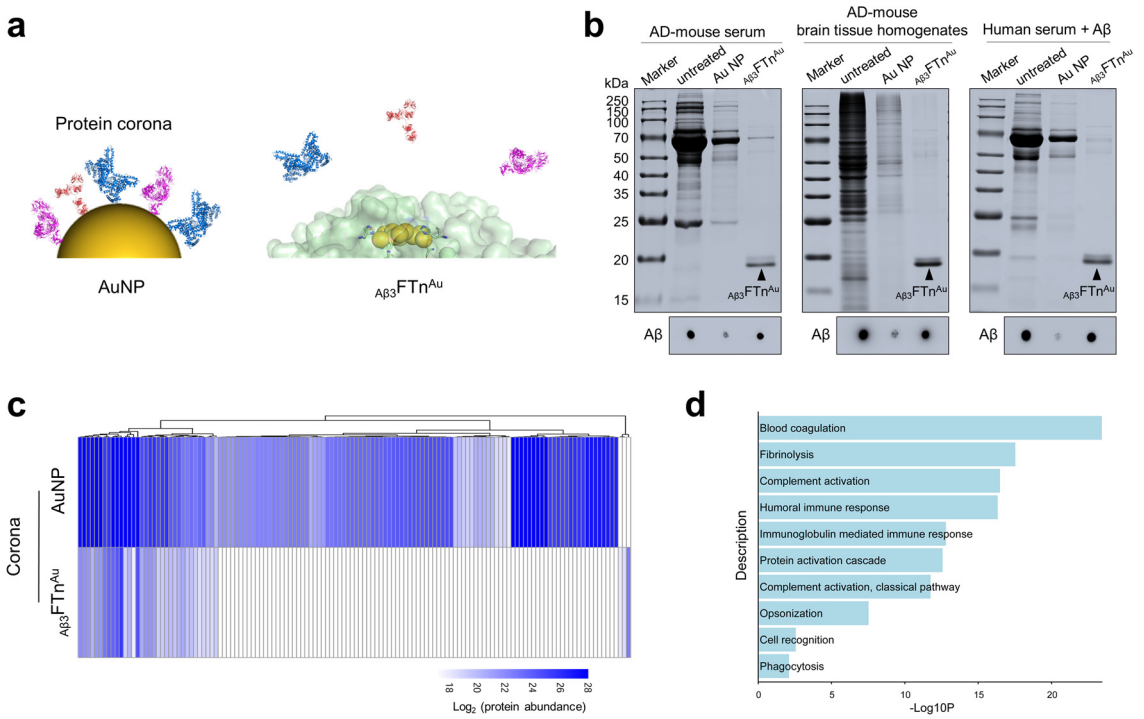

Supplementary Fig. 4. Proteomic characterization of the protein corona associated with bare Au NPs and $_{A\beta3}FTn^{Au}$. (**a**) Schematic illustration of protein corona formation on bare Au NPs and $_{A\beta3}FTn^{Au}$, highlighting the reduced nonspecific adsorption of plasma proteins conferred by the ferritin scaffold. (**b**) SDS-PAGE analysis of protein corona profiles formed on Au NPs and $_{A\beta3}FTn^{Au}$ NPs after incubation with 5×FAD mouse serum, 5×FAD brain homogenates, and human serum supplemented with Aβ standards. Compared with bare Au NPs, $_{A\beta3}FTn^{Au}$ displays negligible protein band signals, indicating substantially reduced nonspecific protein adsorption across different biological environments. (**c**) Heatmap showing the relative abundance of corona-associated proteins identified on bare Au NPs and $_{A\beta3}FTn^{Au}$ by mass spectrometry-based proteomic analysis. (**d**) GOBP enrichment analysis of proteins exclusively identified in the protein corona of bare Au NPs, revealing significant ($P < 0.05$) enrichment of biological pathways associated with immune recognition, coagulation, and phagocytosis, which are commonly implicated in nonspecific uptake and clearance of nanomaterials.

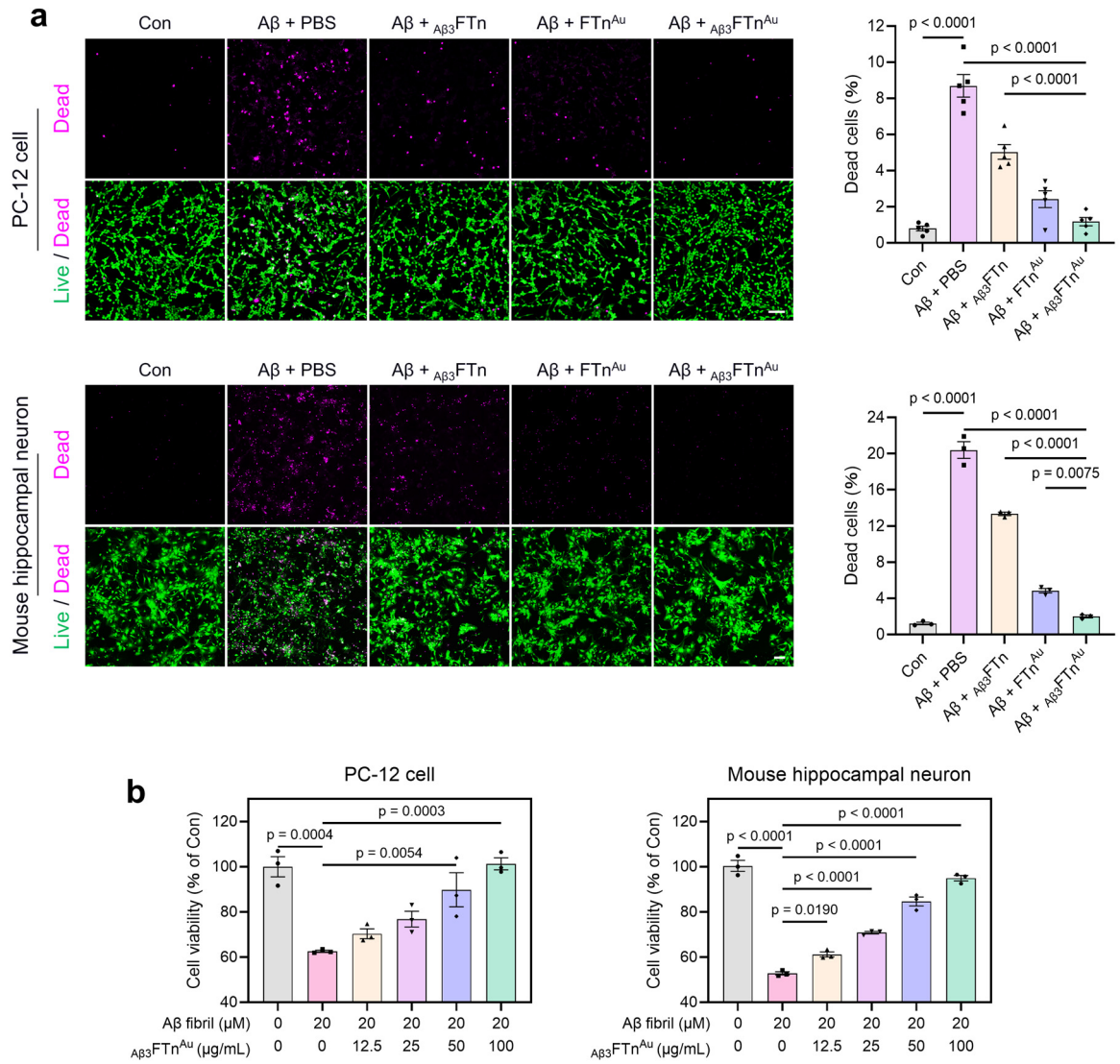

Supplementary Fig. 5. ***In vitro*** **neuroprotective effects of $_{A\beta3}FTn^{Au}$.** (**a**) Representative confocal images of live/dead staining (green: live cells; red: dead cells, left), in PC-12 cells and primary hippocampal neurons, accompanied by quantitative analysis of cell viability (right). Scale bar = 100 μm. (**b**) $_{A\beta3}FTn^{Au}$ mitigates Aβ fibril-induced cytotoxicity in PC-12 cells and primary neurons in a dose-dependent manner. All values were presented as mean ± SEM from three biologically independent experiments. Statistical analyses were conducted using one-way ANOVA for all comparisons.

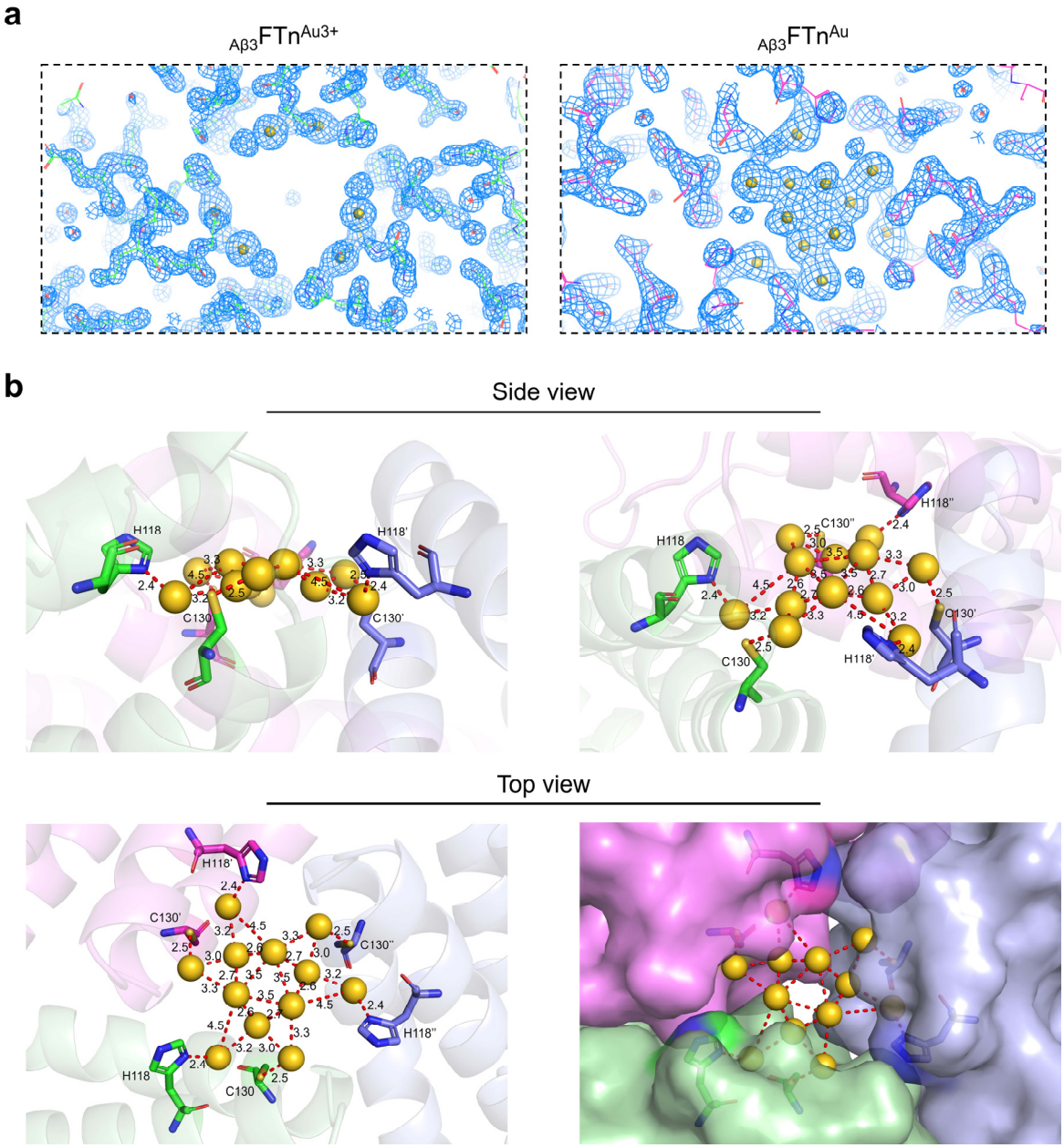

Supplementary Fig. 6. Structural validation and binding site of the sub-nanometric gold cluster within $_{A\beta3}FTn^{Au}$. (**a**) Omit electron density maps of the gold cluster in $_{A\beta3}FTn^{Au3+}$ (left) and $_{A\beta3}FTn^{Au}$ (right) crystal structures. The omit electron density (blue mesh) shows well-resolved and continuous features around Au atoms (yellow spheres) and surrounding coordinating residues, supporting reliable gold placement with minimal model bias. (**b**) Binding site of the sub-nanometric gold cluster within $_{A\beta3}FTn^{Au}$, with selected bond distances labeled. The side view highlights the sheet-like, layered architecture of gold nanocluster, while the top view reveals the spatial arrangement of individual Au atoms and the encapsulating configuration provided by the $_{A\beta3}FTn$ scaffold. Gold atoms are shown as yellow spheres. The Au-Au distances (red dash line) refer to center-to-center measurements.

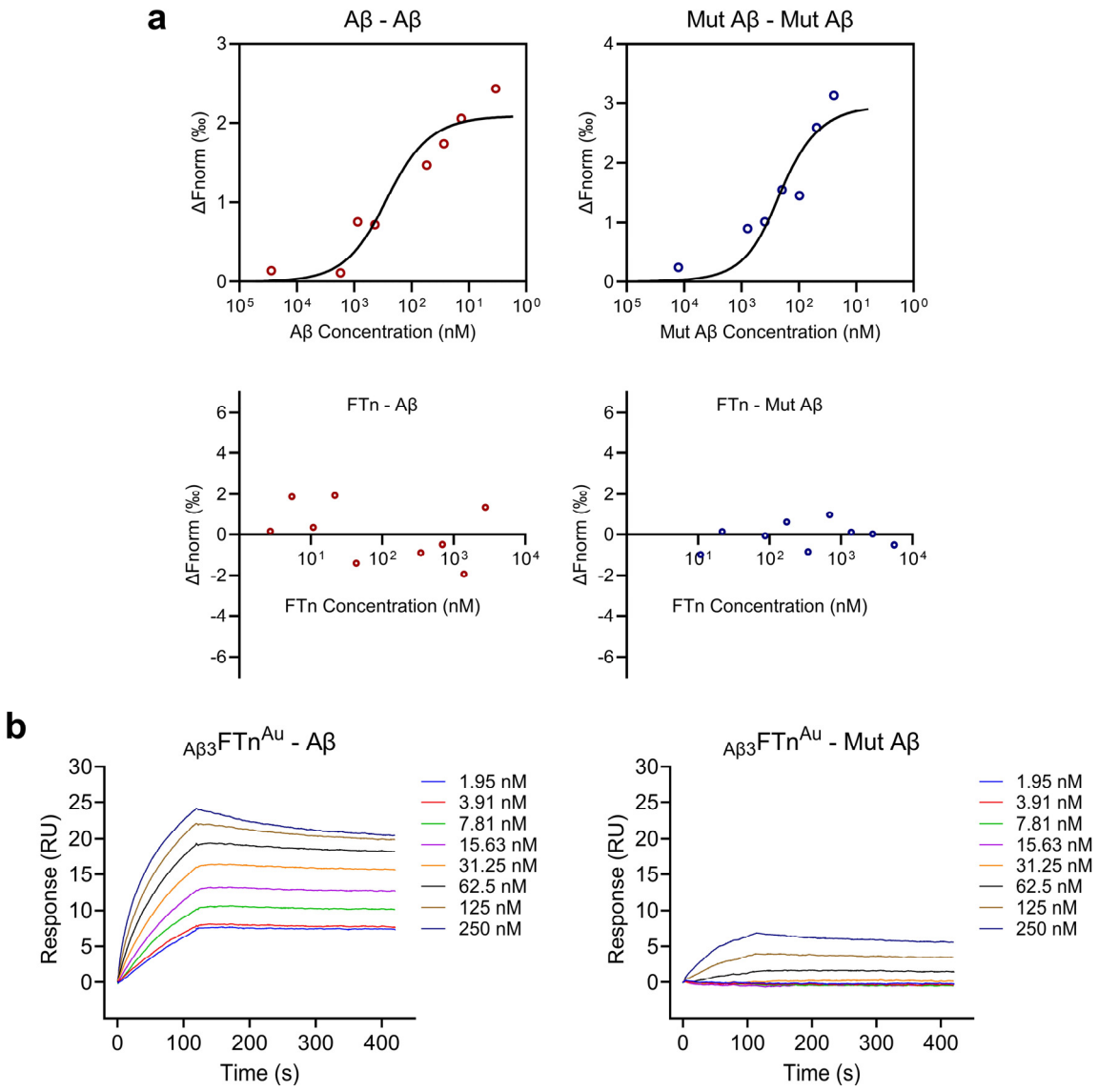

Supplementary Fig. 7. Binding analyses involving Aβ, mut Aβ, and FTn-based constructs. (**a**) MST analysis of binding interactions used as experimental controls. The upper panels show the self-association of wild-type Aβ and mut Aβ, serving as a positive control for aggregation-related binding. The lower panels show MST measurements of interactions between wild-type FTn and Aβ or mut Aβ, serving as a negative control to demonstrate the absence of nonspecific binding. (**b**) SPR analysis indicating strong interaction between $_{Aβ3}FTn^{Au}$ and native Aβ, with substantially weakened binding toward mut Aβ.

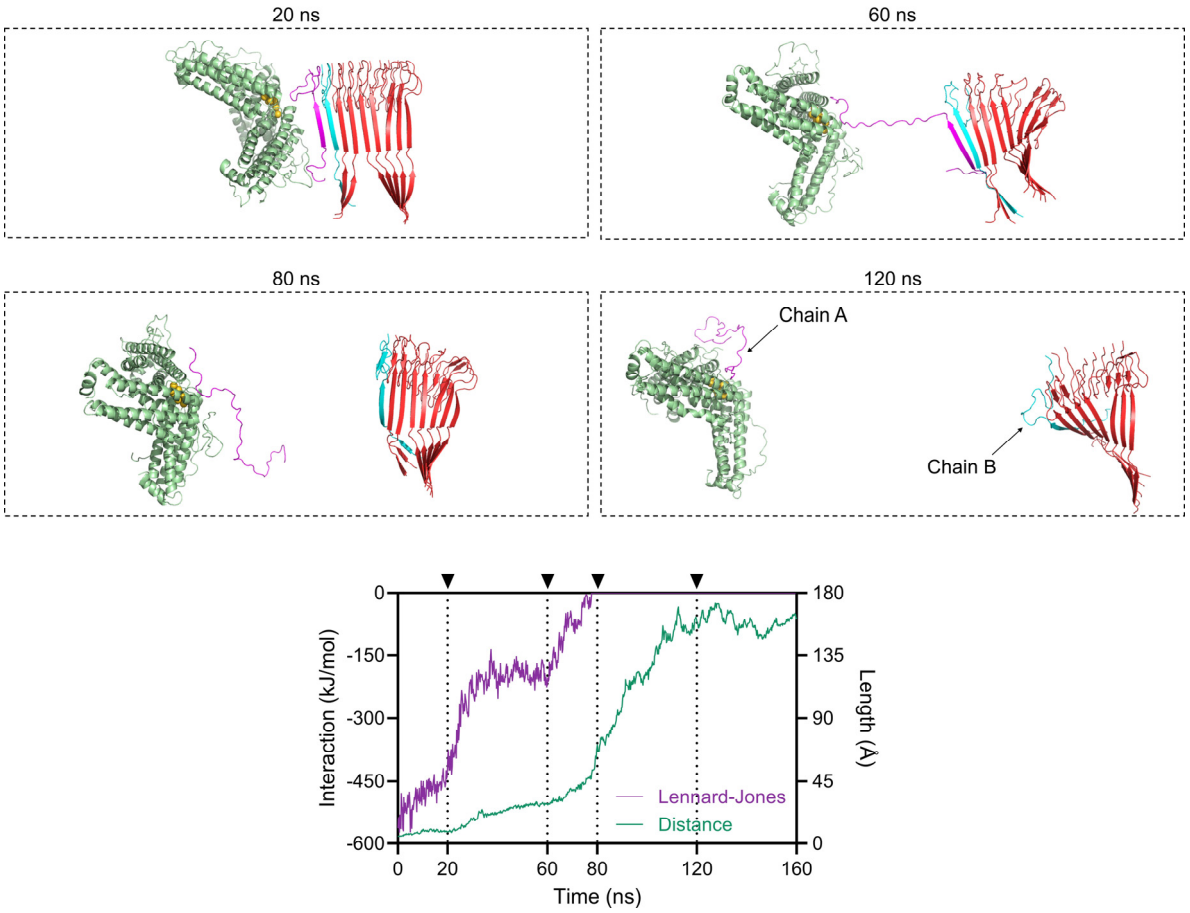

Supplementary Fig. 8. Quantitative analysis of Lennard-Jones potential and inter-chain distance between Chain A (purple) and Chain B (blue) during simulation, supporting the destabilization of Chain A-Chain B inter-monomer interactions by $_{A\beta3}FTn^{Au}$.

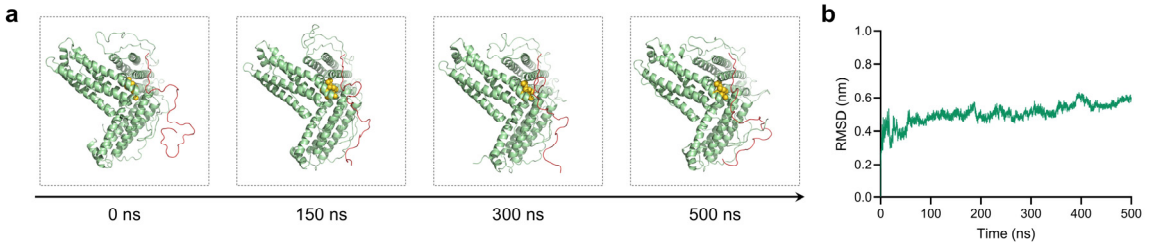

Supplementary Fig. 9. Extended molecular dynamics simulation of the $_{A\beta3}$FTn^{Au}-Aβ complex formed after edge-chain dissociation. (**a**) Representative snapshots of the complex at the indicated time points ($_{A\beta3}$FTn^{Au} shown in green and yellow, Aβ shown in red). (**b**) RMSD of the entire complex over the full 500 ns trajectory.

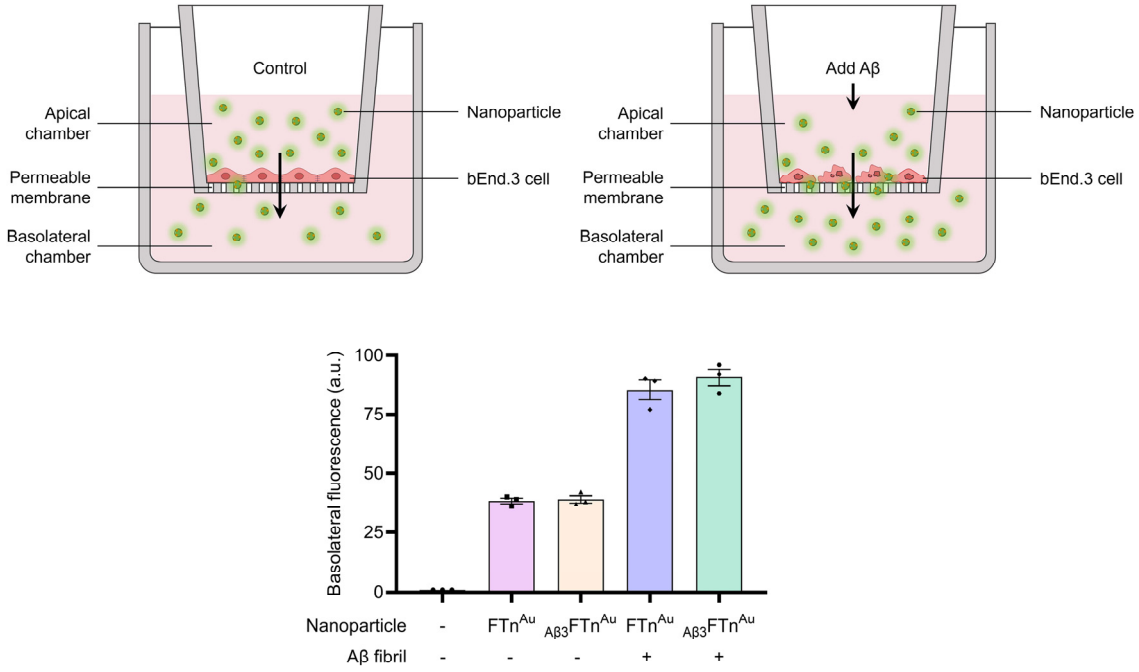

Supplementary Fig. 10. *In vitro* transwell assay for evaluating NP transport across a BBB model. Top, schematic illustration of the transwell-based BBB model and TEER monitoring under control conditions and after Aβ exposure. Bottom, quantitative analysis showing increased translocation of $_{A\beta3}FTn^{Au}$ across the endothelial barrier in the presence of Aβ. Data are presented as mean ± SEM (n = 3 independent transwell inserts per condition).

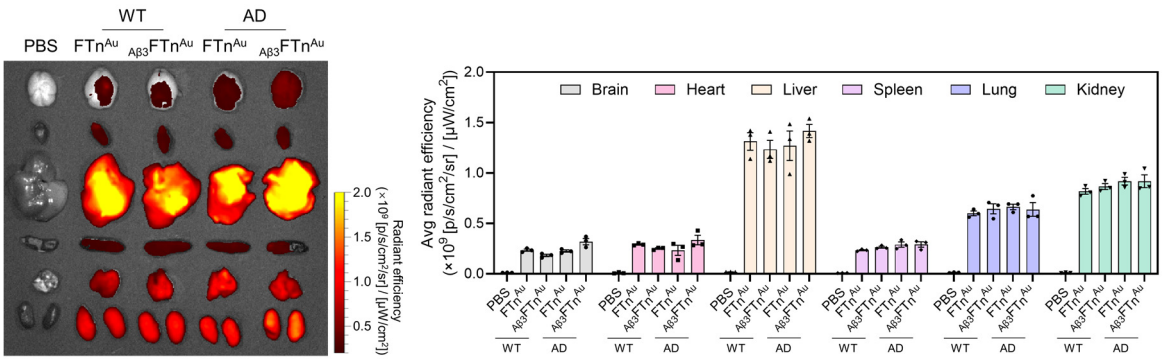

Supplementary Fig. 11. *Ex vivo* fluorescence imaging (left) and corresponding quantitative analysis (right) of major organs at 6 hours post-administration, including brain, heart, liver, spleen, lung, and kidney (n = 3 mice per group). Data are presented as mean ± SEM.

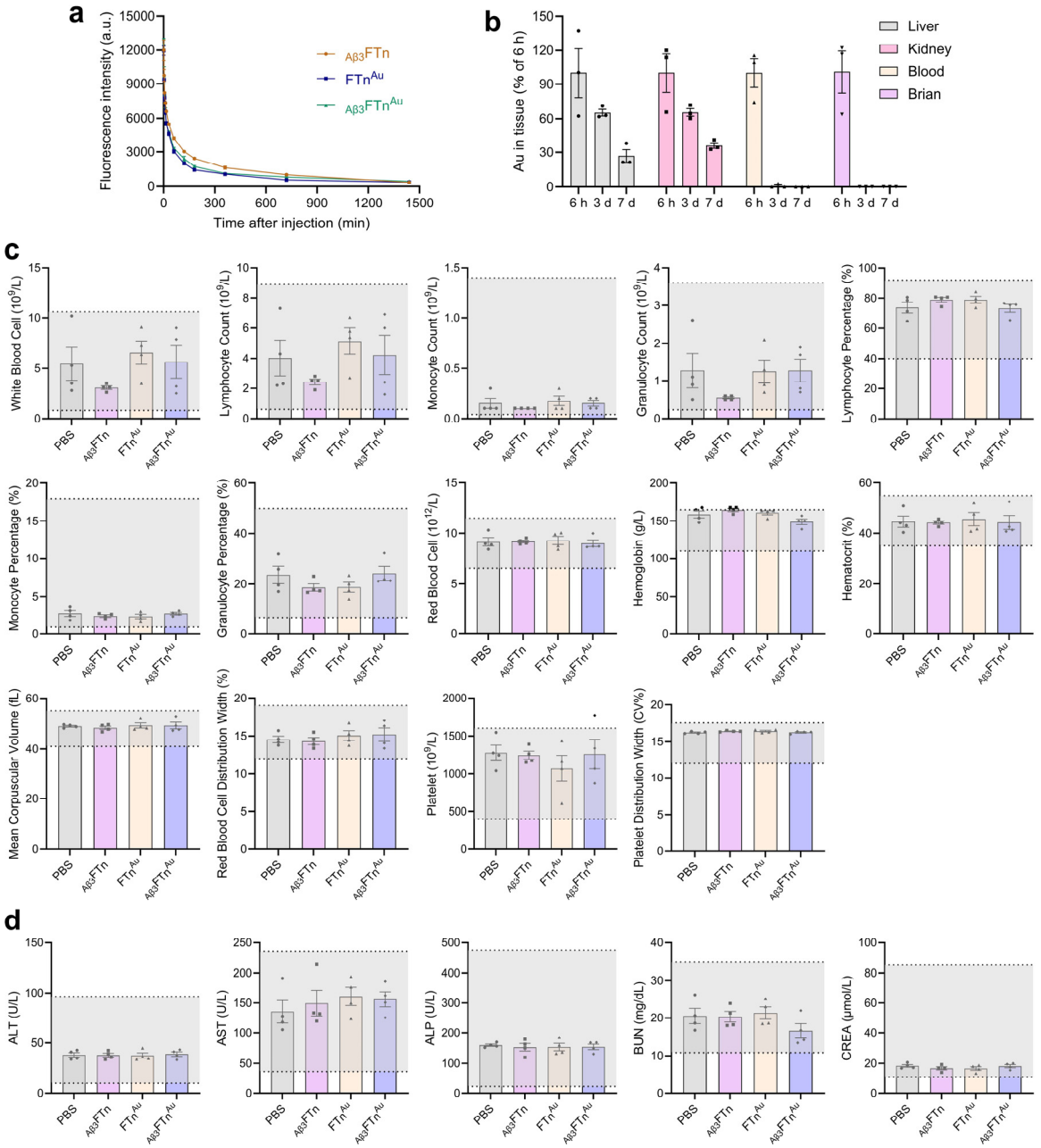

Supplementary Fig. 12. *In vivo* circulation behavior, Au quantification, and systemic safety-related analyses. (**a**) Blood circulation profiles of $_{A\beta3}$FTn, FTn^{Au}, and $_{A\beta3}$FTn^{Au} following systemic administration, showing time-dependent clearance behavior (n = 3 mice per group). (**b**) Quantitative analysis of gold accumulation in the liver, kidney, blood, and brain following systemic administration of $_{A\beta3}$FTn^{Au}, as determined by ICP-OES (n = 3 mice per group). (**c**)-(**d**) Hematological parameters and plasma biochemical markers related to liver and kidney function post-administration (n = 4 mice per group). Values within the normal physiological ranges are highlighted in grey. All values were presented as mean ± SEM.

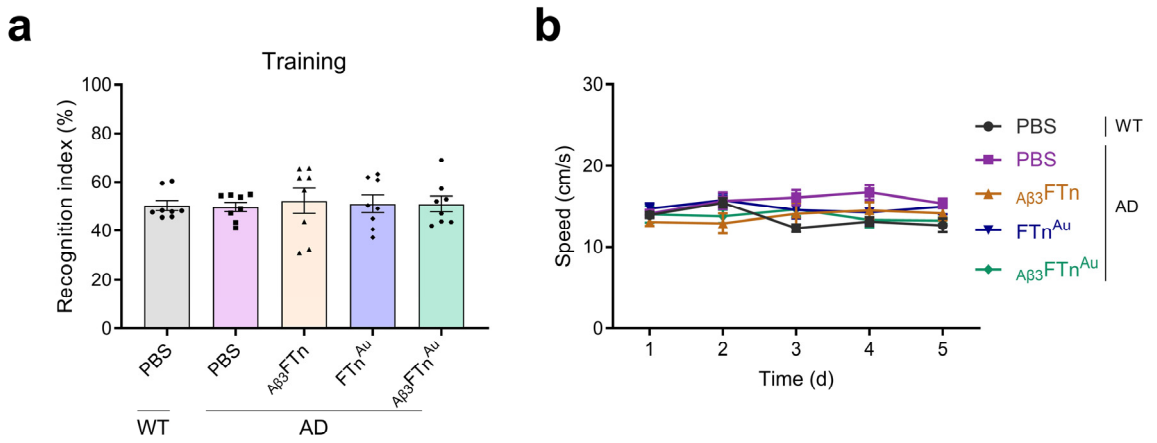

Supplementary Fig. 13. Behavioral baseline assessments in object recognition and water maze tests. (**a**) Recognition index during the training phase of the NOR test, demonstrating no significant differences among groups prior to memory evaluation (n = 8 mice per group). (**b**) Average swimming speed during the training phase of the MWM, indicating comparable motor abilities across all groups (n = 8 mice per group). All values were presented as mean ± SEM. The data were statistically analyzed using one-way ANOVA, and no significant differences were observed.

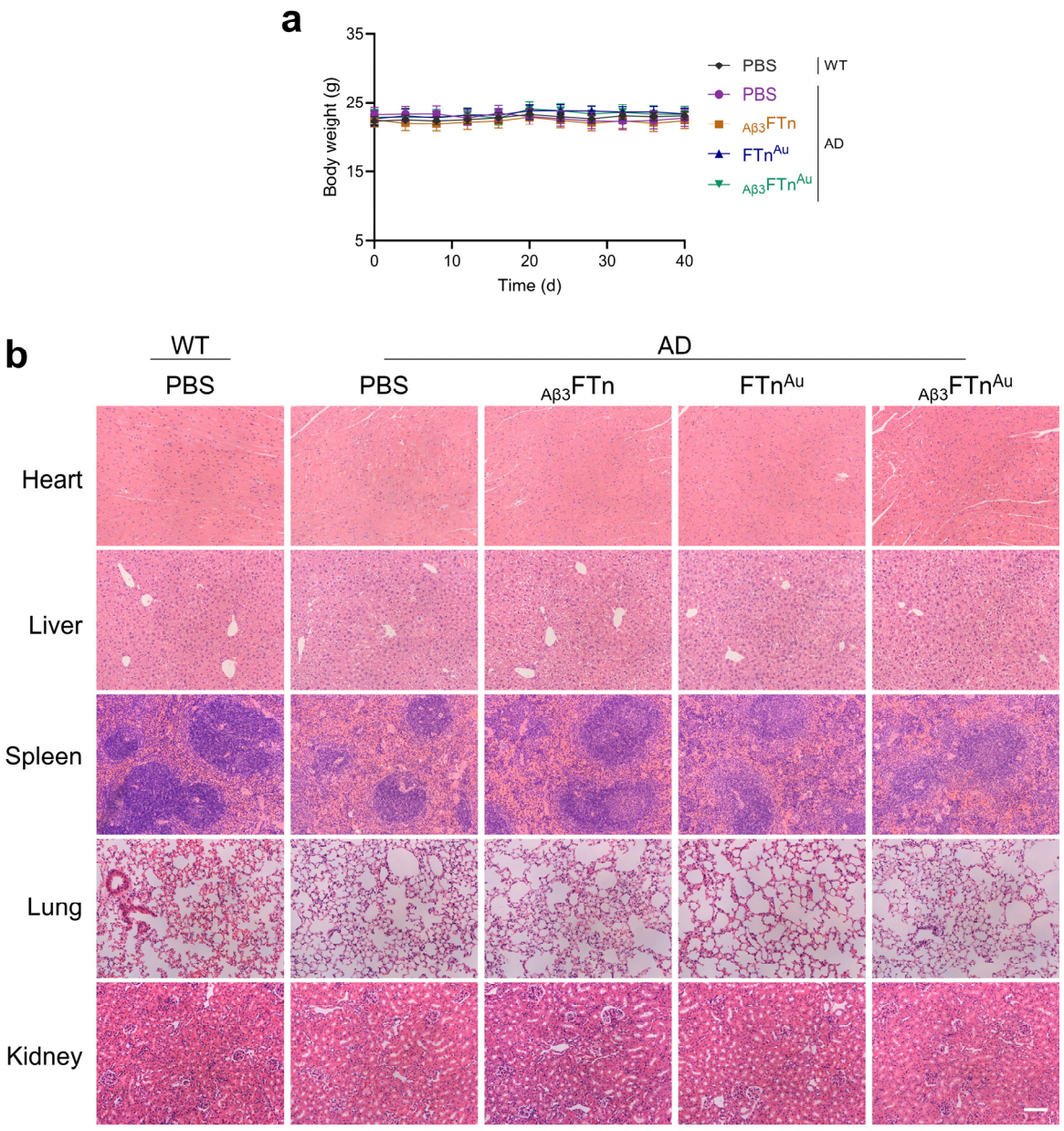

Supplementary Fig. 14. *In vivo* biosafety evaluation of $_{A\beta3}FTn^{Au}$ treatment. (**a**) Longitudinal body weight monitoring across different treatment groups, indicating no significant changes indicative of systemic toxicity (n = 8 mice per group). (**b**) Representative H&E-stained histological images of major organs (heart, liver, spleen, lung, and kidney) post-treatment, showing no evident pathological abnormalities. Scale bar = 100 μm. Images in (**b**) are representative of three mice per group with similar results. All values in (**a**) were presented as mean ± SEM.

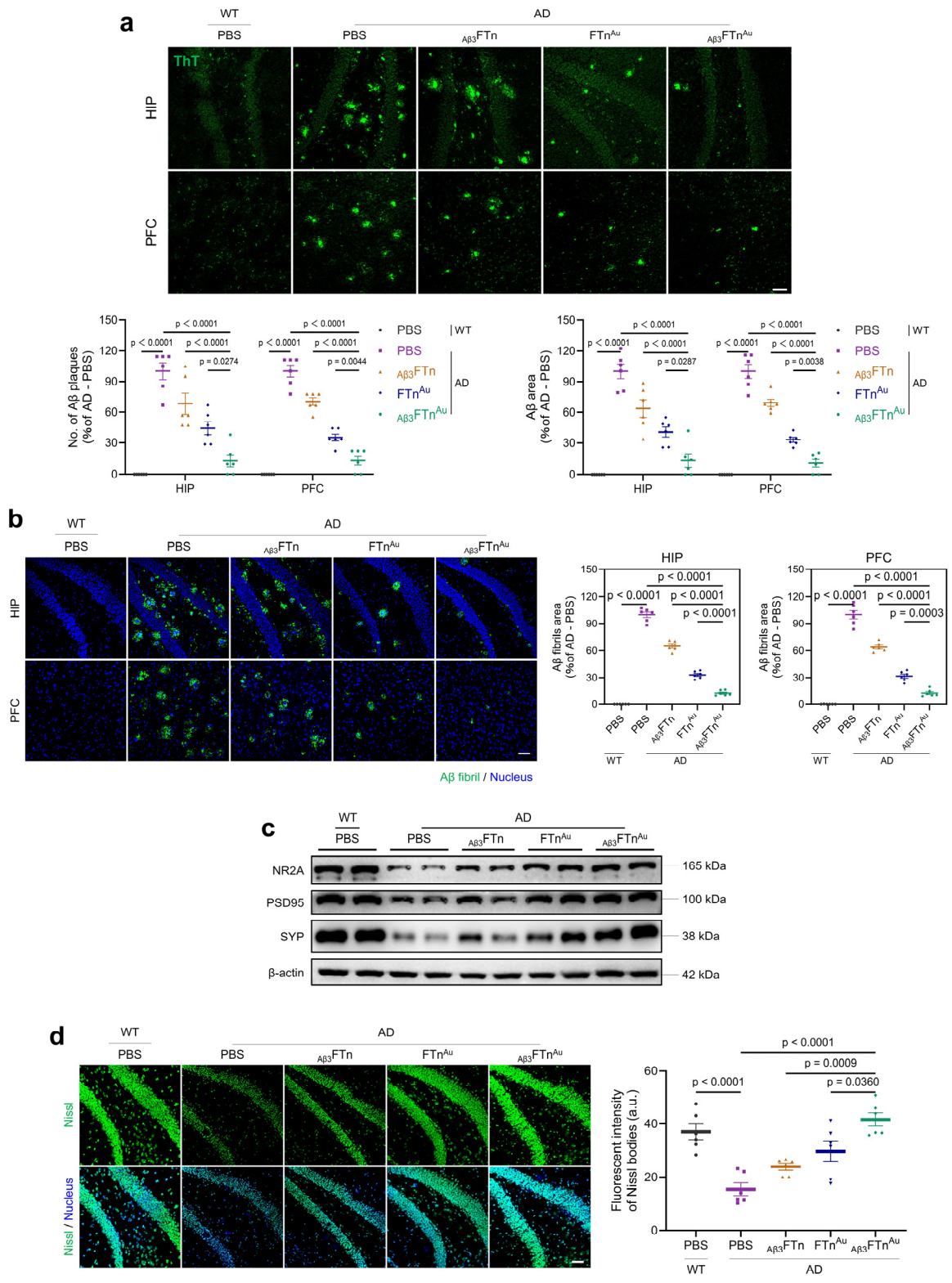

Supplementary Fig. 15. Histological and molecular evaluation of Aβ pathology and synaptic integrity across five treatment groups in 5×FAD mice. (**a**) ThT staining of Aβ plaques (green) in the HIP and PFC of 6-month-old 5×FAD mice across five treatment groups (top), with corresponding quantification (n = 6 technical replicates across three biologically independent experiments) of plaque number and area (bottom). Scale bar = 50 μm. (**b**) Representative immunofluorescence images (left) and corresponding quantification (right)

of Aβ fibrils (green) coverage (n = 6 technical replicates across three biologically independent experiments) in the HIP and PFC following different treatments. Scale bar = 50 μm. (**c**) Western blot analysis of synaptic markers NR2A, PSD95, and SYP in the hippocampal tissue. (**d**) Nissl staining of the HIP from 6-month-old 5×FAD mice in each treatment group (left), with quantitative analysis (n = 6 technical replicates across three biologically independent experiments) of staining intensity (right). Scale bar = 50 μm. All values were presented as mean ± SEM in (**a**)-(**b**) and (**d**). Statistical analyses were conducted using one-way ANOVA for all comparisons.

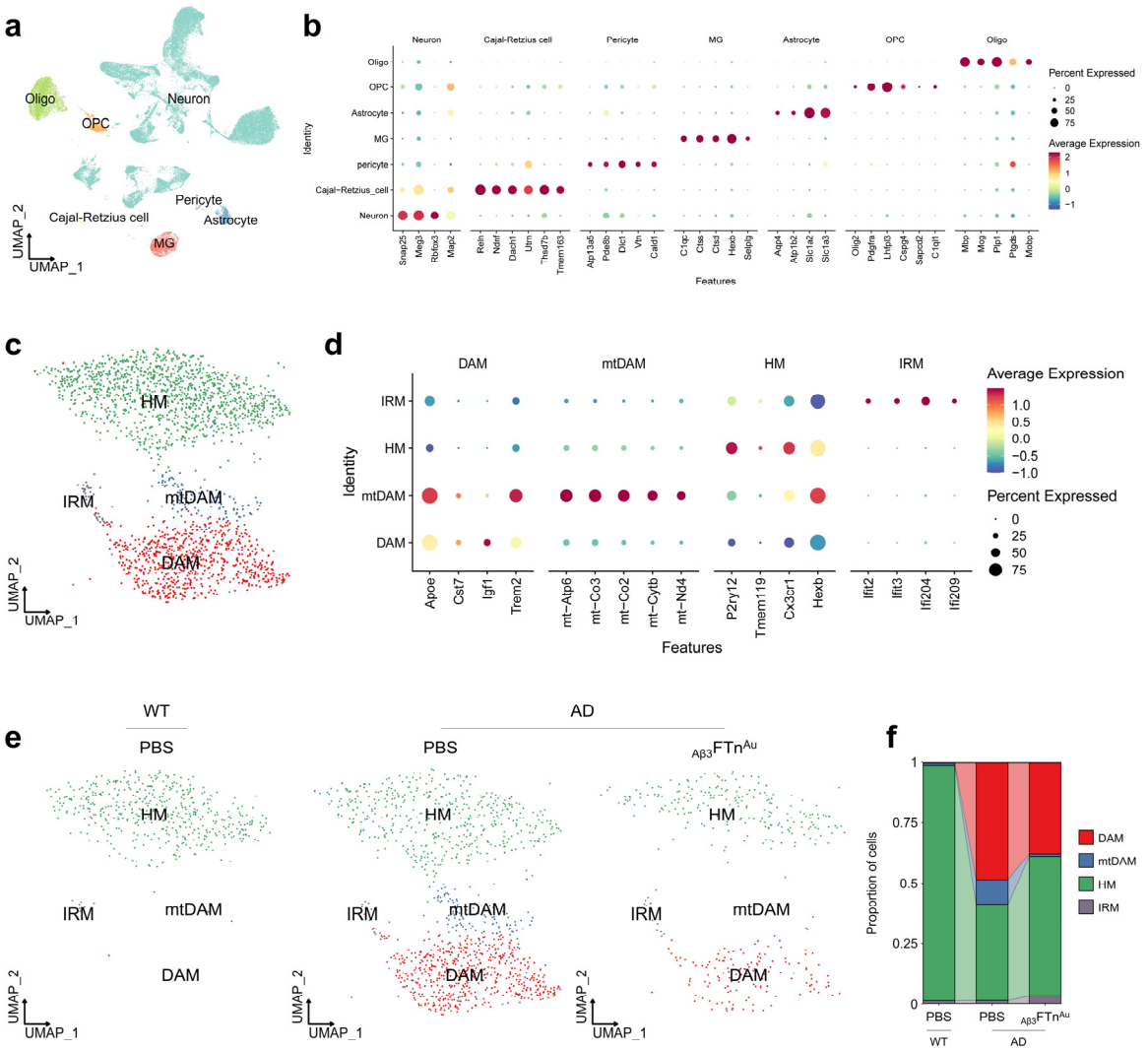

Supplementary Fig. 16. Single-cell profiling of dynamic subtype transitions following $_{A\beta3}FTn^{Au}$ treatment. (**a**) UMAP plot showing integrated clustering and annotation of hippocampal brain cells across all treatment groups. (**b**) Bubble heatmap illustrating the expression of representative marker genes for each major cell type. (**c**) UMAP visualization of distinct microglial subpopulations, including disease-associated microglia (DAM), mitochondrial DAM (mtDAM), homeostatic microglia (HM), and interferon-responsive microglia (IRM). (**d**) Bubble heatmap illustrating key marker gene expression profiles for each microglial subtype. (**e**) UMAP plots displaying the distribution of microglial subclusters within individual treatment groups. (**f**) Bar graph quantifying the relative proportions of each microglial subtype across the three treatment groups. For all panels, n = 2 biologically independent mice per group.

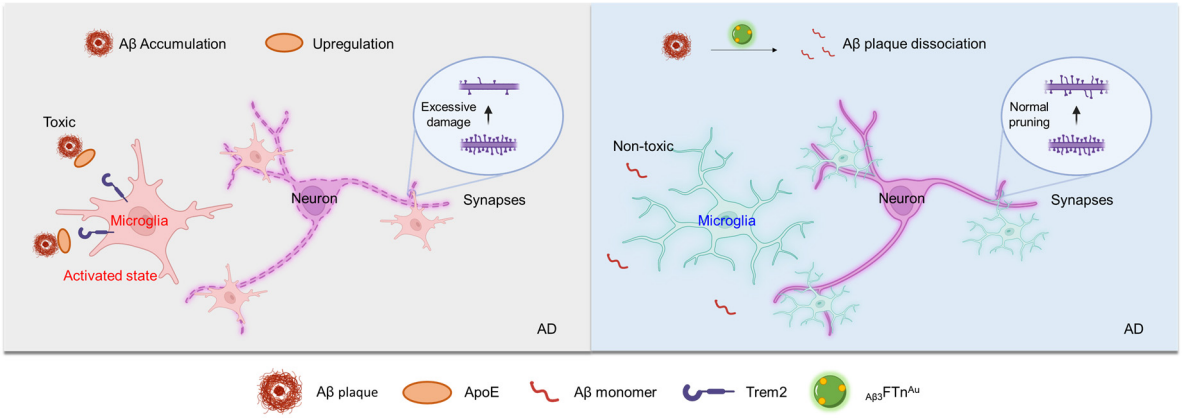

Supplementary Fig. 17. Schematic illustration of the proposed mechanism underlying AD therapy via $_{A\beta3}FTn^{Au}$-mediated Aβ plaque clearance (Major schematic elements were created with biorender.com). Left: Pathological process in AD where Aβ and ApoE contribute to Trem2-mediated microglial activation and excessive synaptic pruning. Right: $_{A\beta3}FTn^{Au}$ promotes Aβ plaque dissociation, thereby mitigating Trem2-mediated microglial activation and reducing aberrant synaptic pruning.

Supplementary Tables

Supplementary Table 1 | Compilation of Aβ-binding peptide sequences and analysis of their binding sites.

$_{A\beta}$FTn constructs	Aβ binding peptides sequence	Binding site	Citations
$_{A\beta1}$FTn	PKLRMKE	N-terminus (D1-K28)	[2]
$_{A\beta2}$FTn	KKKKKG	N-terminus (D1-K28) and C-terminus (A30-V36)	[3]
$_{A\beta3}$FTn	RYYAAFFARR	GAG-binding sites (E11-Q15), Hydrophobic core region (K16-F20) and Turn region or "salt bridge" region (A21-A30)	[4]
$_{A\beta4}$FTn	DFFPL	Hydrophobic core region (K16-F20)	[5]
$_{A\beta5}$FTn	KLVFF	Hydrophobic core region (K16-A21)	[6]
$_{A\beta6}$FTn	KLVFFEEEE	Hydrophobic core region (K16-A21)	[6]
$_{A\beta7}$FTn	KLVFFKKKK	Hydrophobic core region (K16-A21)	[6]
$_{A\beta8}$FTn	TLWYKKY	Hydrophobic core region (K16-A21)	[7]
$_{A\beta9}$FTn	LPFFD	Hydrophobic core region (L17-D23)	[8]
$_{A\beta10}$FTn	EVHHQKLVFF	Turn region or "salt bridge" region (A21-A30)	[9]
$_{A\beta11}$FTn	IGLMV	Turn region or "salt bridge" region (A21-A30)	[10]
$_{A\beta12}$FTn	NAPVSIPQ	Turn region or "salt bridge" region (D23-K28) and C-terminus (G29-M35)	[11]
$_{A\beta13}$FTn	HYYIKKH	C-terminus (G37-A42)	[7]
$_{A\beta14}$FTn	IIGLMVGGVVIA	C-terminus (A30-V36)	[12]
$_{A\beta15}$FTn	CILFWG	Full-length $A\beta_{42}$ peptide	[13]
$_{A\beta16}$FTn	PKRVTYTLNNR VHVQITHTDQKI VYVESSTGDKD AAMTAVKIADE LAKK	Full-length $A\beta_{42}$ peptide	[14]
$_{A\beta17}$FTn	PTLHTHN	Full-length $A\beta_{42}$ peptide	[15]
$_{A\beta18}$FTn	RFRK	Full-length $A\beta_{42}$ peptide	[16]
$_{A\beta19}$FTn	RGPRGRV	Full-length $A\beta_{42}$ peptide	[16]
$_{A\beta20}$FTn	VYIMI	Full-length $A\beta_{42}$ peptide	[13]

Supplementary Table 2 | Crystal structure data collection and refinement statistics. Values in parentheses refer to statistics for the highest-resolution shell.

Parameter	$_{A\beta3}FTn^{Au3+}$ (PDB: 9W28)	$_{A\beta3}FTn^{Au}$ (PDB: 9W29)	mut $_{A\beta3}FTn^{Au}$ (PDB: 9W2A)
Wavelength (Å)	0.979183	0.979183	0.979183
Resolution range (Å)	41.11 - 1.52 (1.574 - 1.52)	32.49 - 1.99 (2.062 - 1.99)	32.4 - 1.55 (1.605 - 1.55)
Space group	F 4 3 2	F 4 3 2	F 4 3 2
Unit cell (Å)	183.8 183.8 183.8 90 90 90	183.7 183.7 183.7 90 90 90	183.2 183.2 183.2 90 90 90
Total reflections	3004167 (232072)	1331428 (102578)	2556204 (136146)
Unique reflections	41405 (4081)	17837 (1588)	38757 (3809)
Multiplicity	72.6 (56.9)	74.6 (64.6)	66.0 (35.7)
Completeness (%)	99.94 (100.00)	93.70 (77.39)	99.94 (99.79)
Mean I/sigma (I)	18.83 (3.37)	13.23 (1.42)	30.23 (1.16)
Wilson B-factor	12.51	22.89	19.05
R-merge	0.2238 (1.771)	0.4081 (4.424)	0.1372 (3.548)
CC1/2	0.999 (0.915)	0.998 (0.903)	1 (0.563)
CC*	1 (0.978)	1 (0.974)	1 (0.849)
Reflections used in refinement	41390 (4081)	17632 (1424)	38745 (3807)
Reflections used for R-free	1975 (189)	907 (80)	1958 (205)
R-work	0.1995 (0.2389)	0.2298 (0.5699)	0.1989 (0.3022)
R-free	0.2094 (0.2376)	0.2585 (0.6145)	0.2059 (0.2963)
CC (work)	0.939 (0.888)	0.920 (0.256)	0.954 (0.779)
CC (free)	0.943 (0.866)	0.939 (0.035)	0.933 (0.736)
Number of non-hydrogen atoms	1554	1524	1605
macromolecules	1418	1418	1410
ligands	8	6	1
solvent	128	100	194
Protein residues	172	172	172
RMS (bonds)	0.007	0.009	0.007
RMS (angles)	0.93	1.05	0.93
Ramachandran favored (%)	98.24	98.82	98.24
Ramachandran allowed (%)	1.76	1.18	1.76
Ramachandran outliers (%)	0.00	0.00	0.00
Rotamer outliers (%)	0.65	0.65	3.31
Clash score	3.22	2.87	3.96
Average B-factor	16.14	26.25	21.55
macromolecules	15.74	25.97	20.51
ligands	15.12	48.05	24.47
solvent	20.64	28.88	29.09

Supplementary Table 3 | Statistical analysis of escape latency during the training phase of the Morris Water Maze (MWM) test, performed using two-way repeated measures ANOVA. *P* values less than 0.05 are highlighted in bold.

Group	Day1	Day2	Day3	Day4	Day5
WT - PBS vs. AD - PBS	0.8470	0.3676	**0.0143**	**<0.0001**	**<0.0001**
WT - PBS vs. AD - $_{A\beta3}$FTn	0.9996	0.9392	0.2044	**0.0002**	**0.0001**
WT - PBS vs. AD - FTn^{Au}	1.0000	0.9974	0.3002	**0.0094**	**0.0104**
WT - PBS vs. AD - $_{A\beta3}$FTn^{Au}	0.9315	0.9777	0.9861	1.0000	1.0000
AD - PBS vs. AD - $_{A\beta3}$FTn	0.7396	0.8172	0.7580	0.4982	0.4342
AD - PBS vs. AD - FTn^{Au}	0.8834	0.5621	0.6233	**0.0466**	**0.0196**
AD - PBS vs. AD - $_{A\beta3}$FTn^{Au}	0.9994	0.1347	**0.0496**	**<0.0001**	**<0.0001**
AD - $_{A\beta3}$FTn vs. AD - FTn^{Au}	0.9984	0.9922	0.9994	0.6989	0.5449
AD - $_{A\beta3}$FTn vs. AD - $_{A\beta3}$FTn^{Au}	0.8548	0.6687	0.4527	**0.0003**	**0.0001**
AD - FTn^{Au} vs. AD - $_{A\beta3}$FTn^{Au}	0.9537	0.8931	0.5911	**0.0099**	**0.0108**

Uncropped blots

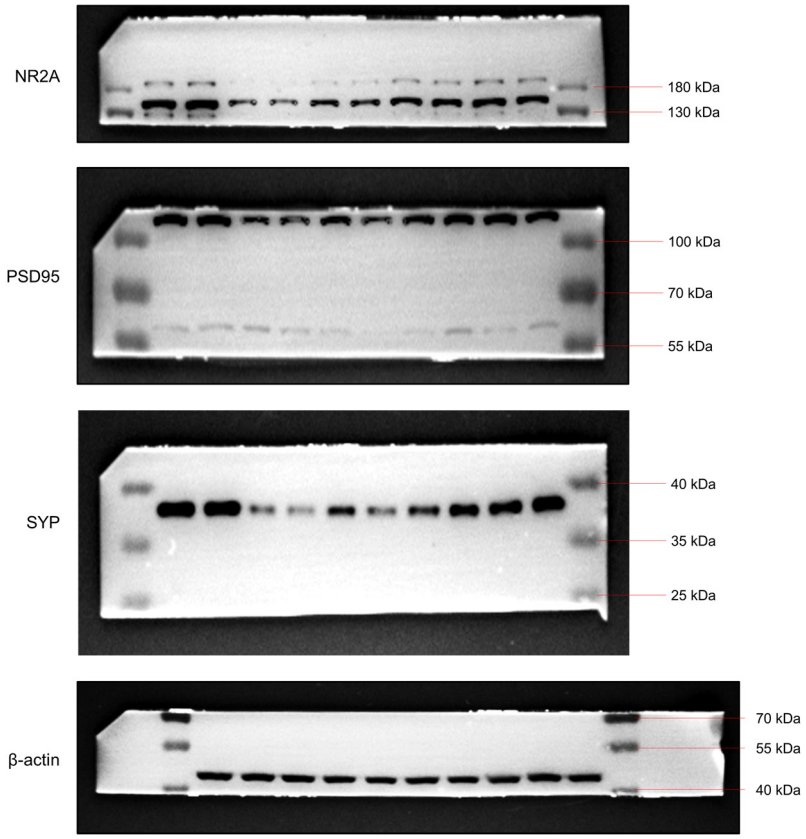

Uncropped and unprocessed Western blot images corresponding to Supplementary Fig. 15c. From top to bottom: NR2A, PSD95, SYP and β-actin. Red lines indicate the positions of molecular weight markers.

References

1 Wang, H. *et al.* Recognition and Removal of Amyloid-β by a Heteromultivalent Macrocyclic Coassembly: A Potential Strategy for the Treatment of Alzheimer's Disease. *Adv Mater* **33**, e2006483, doi:10.1002/adma.202006483 (2021).

2 Sato, W. *et al.* A tailored tetravalent peptide displays dual functions to inhibit amyloid β production and aggregation. *Commun Biol* **6**, 383, doi:10.1038/s42003-023-04771-9 (2023).

3 HochdÖrffer, K. *et al.* Rational design of β-sheet ligands against Aβ42-induced toxicity. *J Am Chem Soc* **133**, 4348-4358, doi:10.1021/ja107675n (2011).

4 Liu, J., Wang, W., Zhang, Q., Zhang, S. & Yuan, Z. Study on the efficiency and interaction mechanism of a decapeptide inhibitor of β-amyloid aggregation. *Biomacromolecules* **15**, 931-939, doi:10.1021/bm401795e (2014).

5 Bhargava, S. *et al.* Microtubule stabilising peptides: new paradigm towards management of neuronal disorders. *RSC Med Chem* **14**, 2192-2205, doi:10.1039/d3md00012e (2023).

6 Lowe, T. L., Strzelec, A., Kiessling, L. L. & Murphy, R. M. Structure-function relationships for inhibitors of beta-amyloid toxicity containing the recognition sequence KLVFF. *Biochemistry* **40**, 7882-7889, doi:10.1021/bi002734u (2001).

7 Lu, J. *et al.* Structure-based peptide inhibitor design of amyloid-β aggregation. *Front Mol Neurosci* **12**, 54, doi:10.3389/fnmol.2019.00054 (2019).

8 Soto, C. *et al.* Beta-sheet breaker peptides inhibit fibrillogenesis in a rat brain model of amyloidosis: Implications for Alzheimer's therapy. *Nat Med* **4**, 822-826, doi:10.1038/nm0798-822 (1998).

9 Fawzi, N. L. *et al.* Structure and dynamics of the Abeta(21-30) peptide from the interplay of NMR experiments and molecular simulations. *J Am Chem Soc* **130**, 6145-6158, doi:10.1021/ja710366c (2008).

10 Cheng, Q. & Qiang, W. Solid-State-NMR-Structure-Based Inhibitor Design to Achieve Selective Inhibition of the Parallel-in-Register β-Sheet versus Antiparallel Iowa Mutant β-Amyloid Fibrils. *J Phys Chem B* **121**, 5544-5552, doi:10.1021/acs.jpcb.7b02953 (2017).

11 Ashur-Fabian, O. *et al.* The neuroprotective peptide NAP inhibits the aggregation of the beta-amyloid peptide. *Peptides* **24**, 1413-1423, doi:10.1016/j.peptides.2003.08.005 (2003).

12 Fradinger, E. A. *et al.* C-terminal peptides coassemble into Abeta42 oligomers and protect neurons against Abeta42-induced neurotoxicity. *Proc Natl Acad Sci U S A* **105**, 14175-14180, doi:10.1073/pnas.0807163105 (2008).

13 Wang, Q. *et al.* De novo design of self-assembled hexapeptides as β-amyloid (Aβ) peptide inhibitors. *ACS Chem Neurosci* **5**, 972-981, doi:10.1021/cn500165s (2014).

14 Murray, K. A. *et al.* De novo designed protein inhibitors of amyloid aggregation and seeding. *Proc Natl Acad Sci U S A* **119**, e2206240119, doi:10.1073/pnas.2206240119 (2022).

15 Zhang, T., Gering, I., Kutzsche, J., Nagel-Steger, L. & Willbold, D. Toward the mode of action of the clinical stage all-d-enantiomeric peptide RD2 on Aβ42 aggregation. *ACS Chem Neurosci* **10**, 4800-4809, doi:10.1021/acschemneuro.9b00458 (2019).

16 Kawasaki, T., Onodera, K. & Kamijo, S. Selection of peptide inhibitors of soluble Aβ(1-42) oligomer formation by phage display. *Biosci Biotechnol Biochem* **74**, 2214-2219, doi:10.1271/bbb.100388 (2010).